Direct Numerical Simulation of Electromagnetic Rough Surface and Sea Scattering by an Improved Banded Matrix Iterative Method

Denis J. Donohue, Hwar-Ching Ku, Donald R. Thompson, and John Sadowsky

A new method for direct numerical simulation of electromagnetic or acoustic wave scattering by randomly rough surfaces is presented. The numerical scheme is derived from the well-known method of moments, in which the surface current integral equation is discretized to form a large matrix inverse problem. The simulations use recent advances in the efficient solution of the inverse problem that exploit the special structure of the moment matrix. By applying specialized numerical techniques, the computing time and memory requirements are reduced, thereby making simulation practical for desktop workstations. As an example, radar sea-scattering simulations are shown that illustrate the diffuse nature of the radar/ocean surface interaction as well as the strong dependence on wind speed and incidence angle. These calculations are particularly relevant to APL programs involving imaging radars and over-water low-elevation-angle target detection and tracking.
(Keywords: Method of moments, Monte Carlo methods, Radar sea scattering, Rough surface scattering.)

INTRODUCTION

The scattering of electromagnetic waves by a randomly rough surface (e.g., the ocean) has long been of interest to APL. Diffuse scattering from the ocean surface can introduce unwanted clutter or noise to radar return and can also affect the signal strength, particularly in low-grazing-angle radars. For imaging radars, such as those used to detect internal waves or ship or submarine surface signatures, the diffusely scattered wave energy represents signal rather than noise. In either case, a clear understanding of the scattering characteristics is needed to model and predict system performance.

APL has made several efforts to physically model radar sea scattering. However, previous approaches have been approximate and limited in their range of validity or applicability to the realistic radar problem. These limitations mirror the extreme difficulty of the problem, which remains a highly active area of research

in electromagnetics.[1] Realizing that the complexity of the problem precludes a general analytical approach, our objective is to develop a powerful and efficient numerical method, with minimal approximations, that has practical application and can be reasonably run on ordinary desktop workstations.

The rough surface scattering problem is illustrated in Fig. 1. An electromagnetic (or acoustic) wave of a general form is incident at angle θ_i to the mean surface normal. The wave scatters diffusely over scattering angle θ_s. The objective is to calculate the amplitude and phase of the scattered field relative to the incident field. Most analytical approaches to the problem calculate this ratio only in the far field; however, our approach is valid at any point above the surface. Since, in practice, the rough surface (e.g., the ocean) may only be statistically defined, statistical moments of the scattered field (usually the mean and standard deviation) become important. The moments are calculated from a numerical approach by a Monte Carlo method, that is, by averaging over repeated random realizations of the surface, each one generated from the same statistical description.

The most common analytical solutions (see Ref. 2 and references therein) to rough surface scattering problems may require the surface to be smooth on the scale of the wavelength λ of the incident field, or perhaps require that fluctuations in surface height from the mean plane are very small compared with the wavelength. Such restrictions can limit our ability to analyze microwave scattering from the ocean, particularly for very low-grazing-angle fields. Several approximate numerical methods have also been developed to extend the limits of analytical theories[3–5]; however, they are often constrained by computational complexity and by the difficulty of quantifying errors.

A promising alternative approach is the method of moments,[6] a direct numerical simulation that generates a solution that is, in principle, exact. The method is based on solving the surface current integral equation by discretizing and reducing the equation to a large matrix inverse problem. In the past, moment methods have been severely limited for practical problems by the extremely large number of unknowns required. Significant progress has been made recently on accelerated solution schemes that take advantage of the structure of the moment matrix as determined by the physics of the scattering problem. For example, the banded matrix iterative approach (BMIA)[7] presented in this article takes advantage of the localized nature of surface current interactions by splitting the full moment matrix into a diagonally dominant, strong interaction matrix and a sparse, weak interaction matrix. The matrix inversion is carried out on the bandwidth-limited strong interaction matrix only, thereby saving considerable computing time and memory.

This article presents an overview of the theoretical development behind the BMIA, along with a discussion of the numerical code and systematic improvements developed by the authors. Numerical results are also presented from random rough surfaces with Gaussian spectra and for 10-GHz radar scattering from random ocean surface realizations. The results are potentially useful for estimating wind-dependent returns from imaging radars or signal characteristics associated with specular reflections in low-grazing-angle radars.

Figure 1. Coordinate system and geometry for modeling wave scattering from a one-dimensional randomly rough surface. The rough surface S (red curve) is described by the height $z = f(x)$ above the mean plane or x axis. A wave field ψ^{inc} is incident at angle θ_i to the mean surface normal. The scattered field ψ^{sc} propagates over a range of scattering angles θ_s ($\mathbf{k}_i$ and $\mathbf{k}_s$ = wavevectors of the incident and scattered fields, respectively).

THEORETICAL DESCRIPTION

A wave field, $\psi^{inc}(\mathbf{r})$, is incident on the rough surface, which is described by a height $z = f(x)$ above a mean plane (Fig. 1). The starting point for the moment method is the surface current integral equation
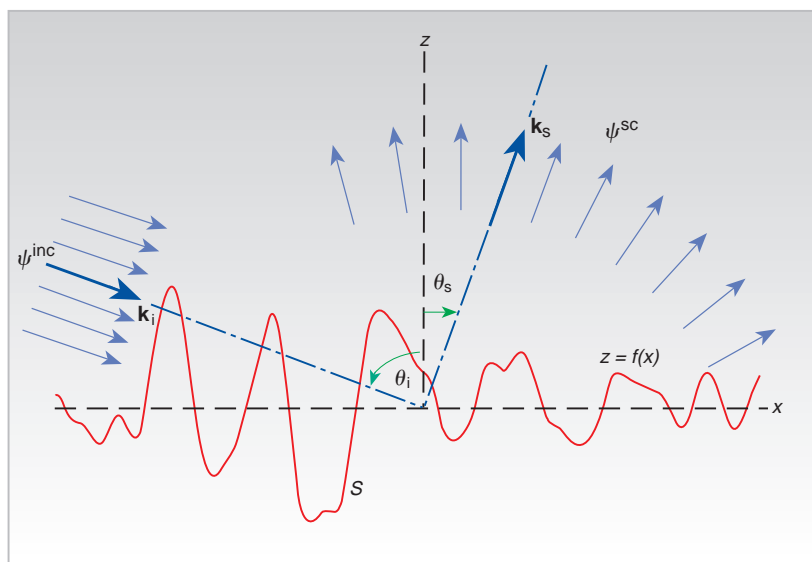
$$0 = \psi^{\text{inc}}(\mathbf{r}) - \int_S G(\mathbf{r}, \mathbf{r}') u(\mathbf{r}') \, dx' \quad \mathbf{r}, \mathbf{r}' \text{ on } S , \quad (1)$$

which is derived by evaluating the standard Helmholtz integral equation *on* the surface S. Here, $G(\mathbf{r}, \mathbf{r}')$ is the free-space electromagnetic Green's function, which in two dimensions (cylindrical geometry) becomes the Hankel function $H_0^{(1)}$ of the first kind, order zero. (This article assumes cylindrical geometry throughout. The extension to three dimensions is discussed in the Summary.) The quantity u under the surface integral is the unknown. For the electromagnetic scattering problem, u is proportional to the induced surface current. Note that Eq. 1 assumes Dirichlet boundary conditions or the equivalent of a horizontally polarized electric field incident on a perfectly conducting surface. More general boundary conditions are discussed later in this article.

The principal idea behind the BMIA is to define a two-point interaction distance r_d that is very large compared with the surface height $f(x)$ everywhere on the solution space. The integral term in Eq. 1 is then split into two integrals, one for source point x' and field point x separated less than r_d (strong interaction) and one for separations greater than r_d (weak interaction). The method of moments solution to Eq. 1, then, consists of discretizing the solution space to form the matrix-vector equation

$$\overline{\overline{\mathbf{Z}}} \, \overline{\mathbf{X}} = \overline{\mathbf{C}} . \quad (2)$$

The source vector $\overline{\mathbf{C}}$ and unknown vector $\overline{\mathbf{X}}$ consist of ψ^{inc} and u evaluated at discrete points $[x_i, f(x_i)]$ and $[x_j, f(x_j)]$, where $x_i = i\Delta$ and Δ is the sampling interval along the x axis. The moment matrix $\overline{\overline{\mathbf{Z}}}$ is the sum of strong and weak interaction matrices, that is, $\overline{\overline{\mathbf{Z}}} = \overline{\overline{\mathbf{Z}}}^{(s)} + \overline{\overline{\mathbf{Z}}}^{(w)}$.

To discretize the strong interaction integral, we assumed that, within each discrete segment $j(i \neq j)$, the argument of the Hankel function, as well as the unknown function u, is effectively constant. This will be true provided the sampling interval Δ is sufficiently small compared with λ. Since the integrand is effectively constant, the moment integral (strong interaction) for source point i and field point j is approximately

$$Z_{i,j}^{(s)} =$$

$$\begin{cases} \dfrac{i\Delta}{4} H_0^{(1)}\left(k\sqrt{(x_i - x_j)^2 + [f(x_i) - f(x_j)]^2} \right) & 0 \leq |x_i - x_j| \leq r_d ; \\ 0 & |x_i - x_j| > r_d , \end{cases}$$
$$(3)$$

where $k = 2\pi\lambda$ is the wavenumber of the radiation field. This result becomes exact in the limit of vanishingly small Δ. When the source and field points coincide $(i = j)$, care must be taken to properly account for the singularity at $x_i = x_j$. The result is similar to Eq. 3.

For the weak interaction matrix, we take further advantage of the problem geometry. Given that the source and field points lie outside the interaction distance r_d, the difference in surface heights $(f_i - f_j)$ is, by definition, much smaller than the separation distance $(x_i - x_j)$. In that case, the Hankel function can be expanded asymptotically as

$$H_0^{(1)}\left(k\sqrt{(x_i - x_j)^2 + [f(x_i) - f(x_j)]^2} \right)$$
$$= \sum_{m=0}^{M} a_m \left(|x_i - x_j| \right) \left[\frac{(f_i - f_j)^2}{(x_i - x_j)^2} \right]^m , \quad (4)$$

where the expansion coefficients a_m can be calculated explicitly to any desired order. For ocean surface radar scattering, we have found that three expansion coefficients $(M = 2)$ are usually sufficient.

With the Hankel function expansion, the weak interaction has a similar asymptotic expansion. In matrix form, the moment integral (weak interaction) in Eq. 1 becomes

$$\overline{\overline{\mathbf{Z}}}^{(w)} = \sum_{m=0}^{M} \overline{\overline{\mathbf{Z}}}_m^{(w)} , \quad (5)$$

where each order $(m = 0, 1, \ldots)$ includes the corresponding expansion term in Eq. 4. From Eqs. 1 and 4, the order zero term, for example, is given by

$$Z_{0_{i,j}}^{(w)} = \begin{cases} 0 & |x_i - x_j| \leq r_d; \\ \dfrac{i\Delta}{4} a_0 (|x_i - x_j|) & |x_i - x_j| > r_d. \end{cases} \quad (6)$$

Equation 2 contains products of the weak interaction matrices, such as $\overline{\overline{\mathbf{Z}}}_0^{(w)}$, with the unknown vector $\overline{\mathbf{X}}$. Since the weak interaction matrix includes all interactions *outside* the separation distance r_d, it will typically be very large and sparse. The matrix-vector product normally requires order N^2 multiplications. However, in this case the expansion of the Hankel function (Eq. 4) about a canonical grid (the mean

plane) results in a cyclically symmetric matrix. As shown in the boxed insert (Efficient Multiplication of a Shift Matrix and a Vector), this matrix-vector product can be computed using a "divide and conquer" strategy that reduces to order $N \log(N)$ operations. For very large systems, the computational time savings can be substantial.

Having covered the construction of the interaction matrices, the next step in the approach is the iterative solution of Eq. 2 for the unknown vector $\overline{\mathbf{X}}$. Our solution involves inverting the dominant, strong interaction matrix only and successively correcting the solution for $\overline{\mathbf{X}}$ by the product with the weak interaction matrix. The iterative technique can be summarized by

$$\overline{\overline{\mathbf{Z}}}^{(s)}\overline{\mathbf{X}}^{(n+1)} = \overline{\mathbf{C}}^{(n)} \quad n = 0,1,2,\ldots, \tag{7}$$

where n represents the iteration number. The vector $\overline{\mathbf{C}}^{(n)}$ is the *updated* source term given by

$$\overline{\mathbf{C}}^{(0)} = \overline{\mathbf{C}}$$

and

$$\overline{\mathbf{C}}^{(n)} = \overline{\mathbf{C}} - \sum_{m=0}^{M}\overline{\overline{\mathbf{Z}}}^{(w)}\overline{\mathbf{X}}^{(n)}. \tag{8}$$

Note from Eq. 7 that the new unknown, $\overline{\mathbf{X}}^{(n+1)}$, is obtained by inverting the banded matrix $\overline{\overline{\mathbf{Z}}}^{(s)}$. The inverse of $\overline{\overline{\mathbf{Z}}}^{(s)}$ can be determined by the standard LU decomposition method, that is, a one-time forward sweep requiring order $b^2N/2$ operations, where b ($b < N$) is the bandwidth as determined by the interaction distance. The stored matrix is then repeatedly used for backward substitution, requiring order $2bN$ operations. Equation 7 is iterated until a convergence criterion is satisfied.

The foregoing discussion is a general description of the BMIA. Recently, we have applied highly specialized numerical methods to the solution of Eq. 2 that further accelerate the iterative convergence and drastically reduce the memory requirement. One technique is a multigrid method (see the boxed insert), designed to address the problem of disparate spatial scales. This method enables us to separately reduce the residual, $\overline{\mathbf{r}} = \overline{\overline{\mathbf{Z}}}\,\overline{\mathbf{X}} - \overline{\mathbf{C}}$, on each of the different grids, which represent successively finer spatial resolution or wavenumber domains (a flowchart showing the interaction between different grid levels is included in the insert). In addition to the multigrid method, we have also employed the so-called preconditioned, generalized

conjugate residual method[12] to further accelerate the convergence at each grid level. Instead of solving the original problem (that is, $\overline{\overline{\mathbf{Z}}}^{(s)}\overline{\mathbf{X}} = \overline{\mathbf{C}}$), we solve the equivalent problem $\overline{\overline{\tilde{\mathbf{Z}}}}^{(s)-1}\overline{\overline{\mathbf{Z}}}^{(s)}\overline{\mathbf{X}} = \overline{\overline{\tilde{\mathbf{Z}}}}^{(s)-1}\overline{\mathbf{C}}$, where $\overline{\overline{\tilde{\mathbf{Z}}}}^{(s)}$ is an approximate operator to $\overline{\overline{\mathbf{Z}}}^{(s)}$. This technique, which further reduces the operation count compared with standard LU decomposition, is also described in the insert.

VALIDATION RESULTS AND ANALYSIS: GAUSSIAN ROUGH SURFACES

Using the foregoing techniques, we now discuss sample calculations of the scattering cross section of random rough surfaces with Gaussian spectra. The incident field can take any form in a moment method solution, but the choice should be one that satisfies Maxwell's equations. The simplest choice, used in most analytical solutions for rough surface scattering, is a uniform plane wave incident at angle θ_i to the mean surface normal. This is not representative of the radar problem, however. A better choice, which approximately satisfies Maxwell's equations, is the tapered plane wave developed by Thorsos.[13] The tapered plane wave has a parameter g, having dimensions of length, that controls the tapering of the incident wave. Typically, if the moment method is solved on a domain of length L, the taper is chosen to be some fraction of L. In this article we use $g = L/4$. This avoids artificial edge diffraction by having the field taper to zero at the edges of the domain. We use the tapered plane wave here as a model of a radar beam originating from a point source located far from the illumination footprint.

Once we calculate the unknown surface current $u(x)$ by the moment method (in discrete form), we can obtain the scattered field at any point above the surface by integrating the product of the surface current with the Green's function, an integral analogous to that shown in Eq. 1 but with the field point $\mathbf{r}$ off the surface. The quantity we consider is the far-field scattering cross section, defined as the ratio of scattered plane wave power propagating far away from the surface to the total power incident on the surface. The expression for the normalized scattering or radar cross section using the tapered plane wave for the incident field is

$$\sigma(\theta_s) = \frac{\left|\int_{-\infty}^{\infty} e^{-ik\alpha(\theta_s,x)}u(x)dx\right|^2}{8\pi gk\sqrt{\pi/2}\cos\theta_i\left(1 - \frac{1+2\tan^2\theta_i}{2k^2g^2\cos^2\theta_i}\right)}, \tag{9}$$

EFFICIENT MULTIPLICATION OF A SHIFT MATRIX AND A VECTOR

A shift matrix is a rectangular matrix in which each row is a shift of the previous row one position to the right, with a new number introduced in the left-most position. Thus, for example, the 3×4 matrix

$$\begin{bmatrix} 3 & 7 & -1 & 0 \\ 4 & 3 & 7 & -1 \\ -9 & 4 & 3 & 7 \end{bmatrix}$$

is a shift matrix. The general shift matrix is an $n \times m$ matrix of the form

$$\overline{\overline{S}} = \begin{bmatrix} b_{m-1} & b_{m-2} & \cdots & b_0 \\ b_m & b_{m-1} & \cdots & b_1 \\ b_{m+1} & b_m & \cdots & b_2 \\ \vdots & \vdots & \cdots & \vdots \\ b_{m+n-2} & b_{m+n-3} & \cdots & b_{n-1} \end{bmatrix}.$$
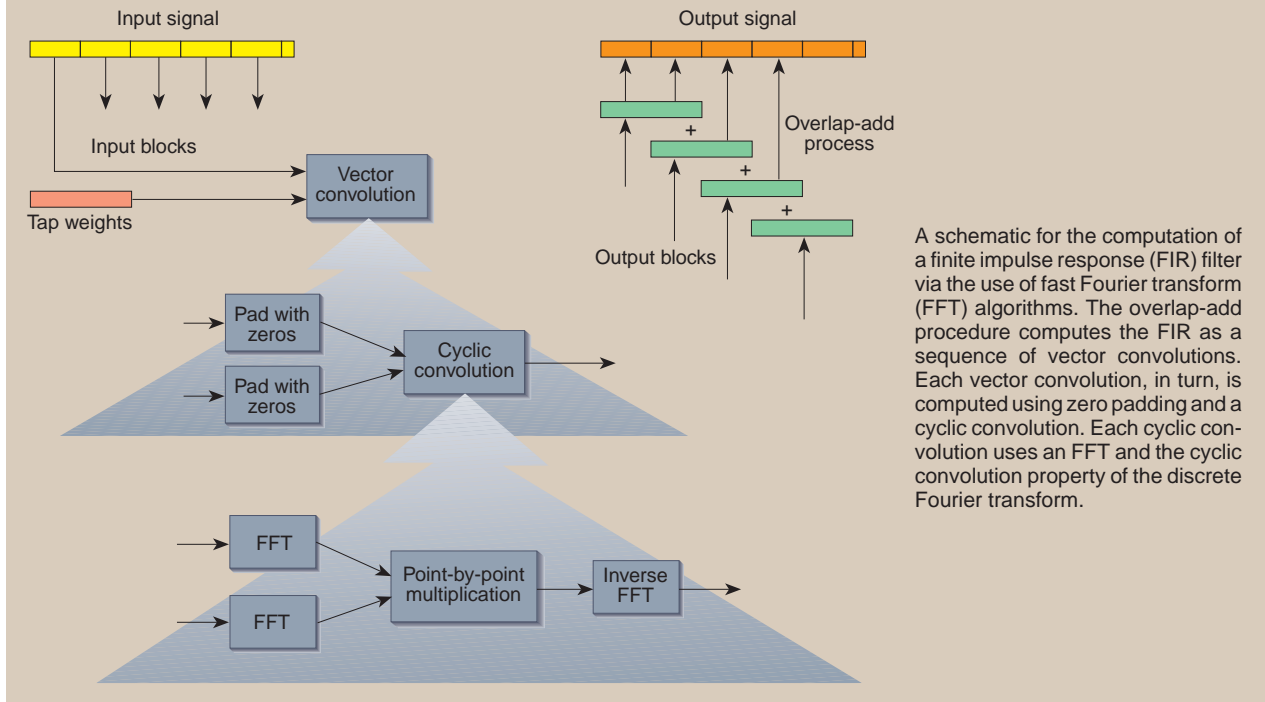
The weak interaction matrices ($\overline{\overline{Z}}^{(w)}$) discussed in the text (see Theoretical Description) are of this form.

Given an m vector $\overline{u}$, we wish to compute the n vector $\overline{x}$ obtained by multiplication with $\overline{\overline{S}}$ as

$$\overline{x} = \overline{\overline{S}}\,\overline{u}.$$

Clearly, the direct computation of $\overline{x}$ uses mn multiplications and $(m-1)n$ additions. This calculation can be made significantly more efficient, however, if one considers that the coordinates of $\overline{x}$ are the output of a finite impulse response (FIR) filter whose tap weights are the coordinates of $\overline{u}$ and whose input signal is $b_0, b_1, b_2, \ldots, b_{m+n-2}$. This filter can be implemented using a fast Fourier transform (FFT) algorithm, which results in an order of magnitude reduction in the arithmetic complexity (i.e., the number of multiplications and additions) of the calculation.

The conversion of the matrix product to an FFT-based filtering is done through a sequence of algorithms (see the figure). First, an FIR filter can be implemented by using a vector convolution process and an algorithm known as an overlap-add procedure (see, e.g., Ref. 8). Basically, the idea is to partition the input signal into nonoverlapping blocks,

A schematic for the computation of a finite impulse response (FIR) filter via the use of fast Fourier transform (FFT) algorithms. The overlap-add procedure computes the FIR as a sequence of vector convolutions. Each vector convolution, in turn, is computed using zero padding and a cyclic convolution. Each cyclic convolution uses an FFT and the cyclic convolution property of the discrete Fourier transform.

where $\alpha(\theta_s, x) = \sin(\theta_s)x + \cos(\theta_s) f(x)$. The integral in Eq. 9 must, of course, be done in discrete form. The *total* scattering cross section σ is also defined as the ratio of the "effective" reflecting area of the surface to the total illuminated area. It is therefore a dimensionless quantity, with a maximum value of 1 corresponding to a perfectly reflecting (lossless) surface. The quantity shown in Eq. 9 is the *differential* scattering cross section, having

units of radian^{-1}. A useful check of the numerical accuracy of our calculation, since the surface is assumed lossless, is to demonstrate that the integral of $\sigma(\theta_s)$ over all scattering angles equals 1. This statement of energy conservation is numerically tested in the following examples.

To generate random rough surfaces, we use a spectral method[13] in which the surface profile is calculated by discrete inverse Fourier transform or fast Fourier

vector-convolve each block with the vector of tap weights, and patch together the output via the overlap-add procedure by adding the head of each subsequent block output to the tail of its predecessor block output.

For the shift matrix multiply, one selects a block size N between m and $(m + n - 1)$. The input signal $b_0, b_1, b_2,..., b_{m+n-2}$, which is formed from the elements of the matrix $\overline{\overline{S}}$, is partitioned into nonoverlapping blocks of size N. The first block is vector-convolved with the vector $\overline{u}$, the first $(m - 1)$ output values from this convolution are discarded, the next $(N - m + 1)$ output values become the first coordinates of the matrix multiply, and the final $(m - 1)$ output values are stored in registers for overlap-add processing. For each subsequent block, the first $(m - 1)$ output values are added to the previous $(m - 1)$ values that were stored for subsequent processing and become the next $(m - 1)$ coordinates of the matrix multiply. The next $(N - m + 1)$ output values are again the next coordinates of the matrix multiply, and the final $(m - 1)$ output values are stored in the registers as before. Processing continues in this fashion until we have the n coordinates of the matrix multiply.

Second, a vector convolution can be computed using a cyclic convolution processor. Here, we are vector-convolving an N vector and an m vector. We expand both vectors into $(N + m - 1)$ vectors by zero-filling on the tail end of each with the appropriate number of zeros. It can easily be shown that the cyclic convolution of the resulting two vectors is equal to the vector convolution of the original vectors.

Finally, the discrete Fourier transform (DFT) satisfies the cyclic convolution property that the DFT of the cyclic convolution of two vectors is the coordinate-wise product of the DFTs of the two vectors. Thus, a fast algorithm for computing the cyclic convolution computes the DFTs of the two input vectors, point-by-point multiplies these two vectors, and computes the inverse DFT of the resulting vector. The three DFTs use the FFT algorithm.

The particular shift matrix (weak interaction) used in this article is a square matrix of size N. For this, we choose a block size N and partition the input into two sets. All FFTs are therefore of size $(2N - 1)$. The vector of tap weights is the same for both input blocks, so its FFT need only be computed once. Thus, five FFTs are used to compute the shift matrix multiply. In addition, we perform $(4N - 2)$ complex multiplications and $(N - 1)$ real additions, yielding the total number of real arithmetic operations (multiplications and additions) of the order $N \log(N)$, rather than N^2, as would be required for the direct calculation.

transform (FFT). The Fourier transform for the individual realization $F(k_j)$ is calculated from the power spectral density $S(k_j)$ according to

$$F(k_j) = [2\pi L S(k_j)]^{1/2}$$

$$\times \begin{cases} [N(0:1) + iN(0:1)]/\sqrt{2} & j \neq 0, N/2; \\ N(0:1) & j = 0, N/2, \end{cases} \quad (10)$$

where L is the length of the realization and for $j < 0$, $F(k_j) = F^*(k_{-j})$, where the asterisk indicates a complex conjugate. The quantity $N(0:1)$, each time it appears, is a random variate: an independent draw from a Gaussian distribution of zero mean and unit variance.

The power spectral density determines the physical characteristics of the rough surface. For Gaussian rough surfaces, the spectrum is Gaussian in k_j and is characterized by the mean squared height $<h^2>$ and surface correlation length l. Equation 10 defines a *random* Fourier transform. Each time it is calculated and inverted, a statistically independent surface realization results. In the Monte Carlo approach, statistical moments of the scattered field are taken over an ensemble of many surface realizations. In this article, we discuss only the mean cross section or ensemble average of Eq. 9.

Sample calculations are now shown for Gaussian surfaces having rms height of 0.5λ and correlation length of 1.0λ. The ensemble-averaged bistatic radar cross section for surfaces of length $L = 40\lambda$ is shown in Fig. 2. In this example, the field is incident at $10°$ from the normal. The result is an average over 4000 realizations of the surface, a very large number that is made possible by the speed of the BMIA code. In Fig. 2, our results are compared against simulation results published by Tsang et al.[7] The comparison is good; the small differences are explained by our use of a more stringent convergence criterion. Note that the peak scattered power in Fig. 2 occurs not in the specular direction but rather in the backscatter direction, $\theta_s = \theta_i = -10°$. The surface, therefore, exhibits enhanced backscattering, an anomalously large return, or retroreflection. This phenomenon has been attributed to a complicated multiple scattering effect that favors phase-coherent paths in the backward direction.[14] The possible relevance of this effect to sea spikes (i.e., anomalously large and transient radar returns from the ocean) is currently under investigation.

Figure 3 shows scattering results from surfaces with similar statistics for a very low grazing angle ($\theta_i = 85°$). The surface length used is a very large 1200λ, which is necessitated by the physics of very low-grazing-angle scatter. At such angles, a finite-width beam has a very large horizontal projection. Furthermore, the incident wave can be multiply-scattered and can induce surface currents well outside the projected footprint. Comparison of Figs. 2 and 3 demonstrates the substantial difference between low-grazing-angle and near-normal incidence rough surface scattering; i.e., whereas Fig. 2 shows broad, diffuse scatter with a slight enhancement in the backscatter direction, Fig. 3 shows a sharp, specular ($\theta_s = \theta_i = 85°$) peak or mirror-like reflection. This

MULTIGRID METHOD

Elliptic and hyperbolic partial differential and integral equations are common in engineering and physics and require extensive numerical computations. Often, the problems exceed the computer's memory capacity or require prohibitive amounts of computing time. The multigrid method[9,10] has emerged as an important advance in algorithmic efficiency that greatly expands the range of problems one can compute. The solution is not generated on a single-grid basis but rather on a multigrid basis, i.e., a sequence of grids spanning the finest grid spacing Δ to the coarsest spacing $2^p\Delta$, where p is the grid level.

For the banded matrix problem, we use "standard coarsening," which involves doubling the mesh from one grid to the next-coarsest grid and also smoothing the residual $(\bar{\mathbf{r}} = \bar{\bar{\mathbf{Z}}}\bar{\mathbf{X}} - \bar{\mathbf{C}})$ to the next-coarsest grid (a process known as restriction). The problem is solved on the coarse grid (low-resolution or small-wavenumber domain), and the coarse-grid correction for the variable transfers the correction back (prolongation) to the fine grid (large-wavenumber domain) to gain rapid convergence (see the accompanying flowchart). The multigrid method lets us reduce the residual on the different frequency domains. On the coarse grid (level $p + 1$), the equation solved is an approximation to the fine-grid (level p) equation. The interaction between the fine grid and the coarse grid can be symbolically correlated by

$$\bar{\bar{\mathbf{Z}}}_{p+1}\bar{\mathbf{X}}_{p+1} - \bar{\bar{\mathbf{Z}}}_{p+1}(\bar{\bar{\mathbf{I}}}_{p+1}^p\bar{\mathbf{X}}_p) = \bar{\bar{\mathbf{I}}}_{p+1}^p\bar{\mathbf{r}}_p . \qquad (A)$$

Here, $\bar{\bar{\mathbf{Z}}}_{p+1}$ represents the operator of Eq. 4 (see text) on the coarse grid, $\bar{\bar{\mathbf{I}}}_{p+1}^p$ is an interpolation operator (restriction) from the fine grid "p" to the coarse grid "$p + 1$," and $\bar{\mathbf{X}}_p$ and $\bar{\mathbf{r}}_p$ are the unknown vector and residual, respectively, on the fine grid. Note that $\bar{\mathbf{r}}_0 = \bar{\mathbf{C}} - \bar{\bar{\mathbf{Z}}}_0\bar{\mathbf{X}}_0$ corresponds to the residual on the finest grid (the original problem). The left-hand side of Eq. A is the difference between the coarse-grid operator acting on the coarse grid and the coarse-grid operator acting on the interpolated fine grid (which is held fixed). After the fine-grid solution has been found, the residual $\bar{\mathbf{r}}_p$ will be zero and the solution of Eq. A becomes

$$\bar{\mathbf{X}}_{p+1} = \bar{\bar{\mathbf{I}}}_{p+1}^p\bar{\mathbf{X}}_p , \qquad (B)$$

as required for convergence. When the residual is nonzero, the left-hand side of Eq. B acts as a forcing term for the

Grid level
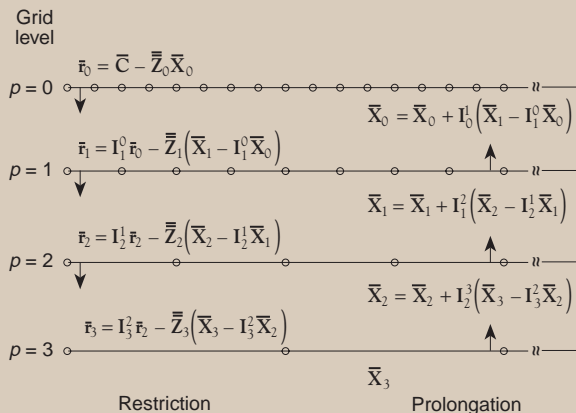
coarse-grid correction, and the correction to $\bar{\mathbf{X}}_{p+1}$ must be transferred back (prolongated) to the fine grid, i.e.,

$$\bar{\mathbf{X}}_p^{\text{new}} = \bar{\mathbf{X}}_p^{\text{old}} + \bar{\bar{\mathbf{I}}}_p^{p+1}\left(\bar{\mathbf{X}}_{p+1} - \bar{\bar{\mathbf{I}}}_{p+1}^p\bar{\mathbf{X}}_p^{\text{old}}\right), \qquad (C)$$

where "new" represents the updated information during the multigrid iterative solution. This prolongation is vital to the success of the scheme. Changes in the variables are transferred back to the fine grid rather than the variables themselves. Both $\bar{\bar{\mathbf{I}}}_p^{p+1}$, the prolongation operator from the coarse grid to the fine grid, and $\bar{\bar{\mathbf{I}}}_{p+1}^p$, the restriction operator from the fine grid to the coarse grid, can be simply constructed through linear interpolation.[11]

Implementing the multigrid algorithm in conjunction with the preconditioned generalized conjugate residual (GCR) method at each grid level is also crucial to the success of the algorithm, not only to accelerate convergence but also to reduce the working space. Before starting the multigrid iteration, the residual on the grid $p = 0$ is first smoothed and estimated, then restricted to the next-finest grid level. Given Eq. A, on the coarse grid $(p + 1)$ we must solve

$$\bar{\bar{\mathbf{Z}}}_{p+1}(\bar{\mathbf{X}}_{p+1} - \bar{\bar{\mathbf{I}}}_{p+1}^p\bar{\mathbf{X}}_p) = \bar{\bar{\mathbf{I}}}_{p+1}^p\bar{\mathbf{r}}_p . \qquad (D)$$

With the definition $\Delta\bar{\mathbf{X}}_{p+1} = \bar{\mathbf{X}}_{p+1} - \bar{\bar{\mathbf{I}}}_{p+1}^p\bar{\mathbf{X}}_p$, the iterative solution of Eq. D by the preconditioned GCR method is

$$\bar{\bar{\mathbf{Z}}}_{p+1}^{(s)}\Delta\bar{\mathbf{X}}_{p+1}^{n+1} = \bar{\bar{\mathbf{Z}}}_{p+1}^{(s)}\Delta\bar{\mathbf{X}}_{p+1}^n + \alpha(\bar{\bar{\mathbf{I}}}_{p+1}^p\bar{\mathbf{r}}_p - \bar{\bar{\mathbf{Z}}}_{p+1}\Delta\bar{\mathbf{X}}_{p+1}^n), \quad (E)$$

where n is the iteration number at each grid level, and α is a free parameter whose optimal value can be determined by minimizing a functional.[12] The coarse-grid operator $\bar{\bar{\mathbf{Z}}}_{p+1}$ is constructed based on the grid spacing Δ_{p+1}, and the preconditioned operator $\bar{\bar{\mathbf{Z}}}_{p+1}^{(s)}$ is a matrix with a truncated bandwidth (the strong interaction) whose storage space is much smaller than that for $\bar{\bar{\mathbf{Z}}}_{p+1}^{(s)}$. This is the critical step for reducing the total storage space for all $\bar{\bar{\mathbf{Z}}}_p^{(s)}$, $p = 1,2,...,J$. On the coarsest grid J, $\bar{\bar{\mathbf{Z}}}_J^{(s)}$ should be reasonably set equal to $\bar{\bar{\mathbf{Z}}}_J^{(s)}$ to ensure fast convergence.

When the coarse-grid correction process transfers the correction from grid level $p + 1$ to p, Eq. D can be written as

$$\Delta\bar{\mathbf{X}}_p^{\text{new}} = \Delta\bar{\mathbf{X}}_p^{\text{old}} + \bar{\bar{\mathbf{I}}}_p^{p+1}\Delta\bar{\mathbf{X}}_{p+1}^{\text{old}} \qquad (F)$$

for $p > 0$ and

$$\bar{\mathbf{X}}_0^{\text{new}} = \bar{\mathbf{X}}_p^{\text{old}} + \bar{\bar{\mathbf{I}}}_0^1\Delta\bar{\mathbf{X}}_1^{\text{old}} \qquad (G)$$

for $p = 0$. Note that the superscript "new" becomes "old" if it is being used to update the information. The order in which the grids are visited is called the multigrid cycle. (For comparisons among different cycles, see Ref. 11.) The calculations in this article use the W cycle. For one multigrid iteration, the coarse-grid correction process transfers the correction back to the finest-grid level, $p = 0$. If the residual does not meet the convergence criterion $(\|\bar{\mathbf{r}}_0\| < \epsilon)$, the multigrid iteration is repeated until the convergence check is satisfied.
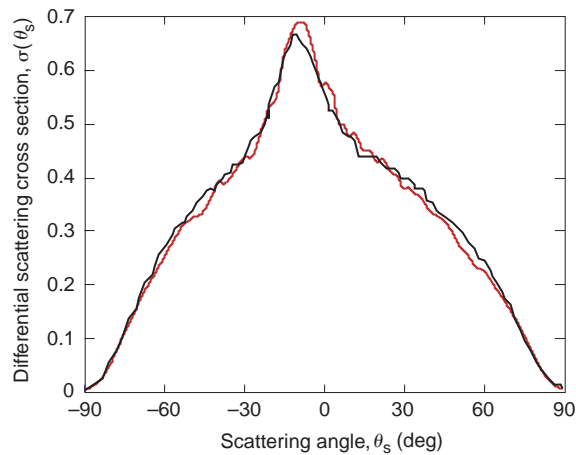
Figure 2. Calculation of the ensemble-averaged, normalized radar cross section from a Gaussian rough surface with rms height of 0.5λ and correlation length of 1.0λ. The incidence angle is 10°, and the result is averaged over 4000 realizations. The banded matrix iterative method results (red) are compared with those published by Tsang et al.[7]

Figure 3. Same as Fig. 2, but for an incidence angle of 85° (near grazing). The surface length is increased to 1200λ, and the result is averaged over 50 realizations.

exemplifies the well-known result that all rough surfaces reflect specularly in the grazing limit, as evidenced by examining the glossy reflection from a sheet of paper viewed "edge on." Note that although the differential cross section in Fig. 3 becomes large near the specular direction, the total cross section, or integral of $\sigma(\theta_s)$ over all scattering angles, is a conserved quantity. In fact, in the limit of a flat surface with a plane wave incident, $\sigma(\theta_s)$ becomes a delta function, singular at θ_i.

Figure 3 was calculated with a sampling rate of 10 points per wavelength. The linear system, therefore, consisted of N = 12,000 unknowns. A problem of this size requires 116 MB of computer memory using the single-grid technique discussed earlier. By using a four-grid decomposition, the memory requirement is reduced to 31 MB. Because of the time and memory required, the problem was not run with the single-grid method. The four-grid solution required 195 min of computer time for one realization of the surface on a 99-MHz workstation. Although this is substantially longer than the 40λ case shown in Fig. 2, we averaged over 50 realizations to obtain reasonable ensemble statistics. The result thus demonstrates the capability of the BMIA code to simulate very low-grazing-angle scatter and to integrate over very large surfaces, both of which are required for many problems of practical interest.

SEA SCATTERING SIMULATIONS

Although the previous discussion demonstrates the capability of the BMIA code on a well-studied class of rough surfaces, our objective is to apply the method to the problem of radar/ocean surface interaction, which
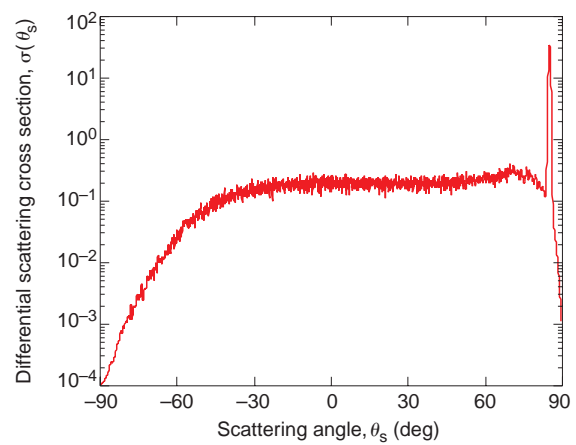
presents many challenges. A primary difficulty is accounting for the tremendous range of spatial scales on the ocean surface (see the boxed insert, Ocean Surface Hydrodynamics). Whereas diffuse scattering is primarily due to roughness scales comparable to or smaller than the radar wavelength (which typically falls in the gravity–capillary portion of the surface spectrum), the larger scales (gravity waves) contribute through tilt, mean curvature, and shadowing effects. In addition, while the radar is sensitive to the small scales, the illumination footprint may be quite large by comparison. This problem is similar to the one addressed by Fig. 3, where the integration domain is very large compared with the wavelength. In many radar/sea scattering problems, however, the situation can be far more extreme than in Fig. 3, particularly at low grazing angles.

Although the BMIA calculation is not a comprehensive solution to the sea scattering problem, tremendous progress has been made in developing an increasingly more realistic simulation. For example, the multigrid method discussed previously has been used to reduce the memory requirement of the problem from the level of large supercomputers to that of typical desktop workstations. Moreover, the speed of the simulation makes it practical to do reasonable amounts of statistical averaging.

Unfortunately, even with a fully capable numerical method, a realistic simulation requires a detailed and accurate model of the ocean surface, and no such model exists. Although approximate, the best models use a linear spectral method similar to that presented in the previous section. As noted earlier (Ocean Surface Hydrodynamics insert), the spectral method has several

OCEAN SURFACE HYDRODYNAMICS

The broadband structure of the ocean surface, with roughness scales spanning many orders of magnitude, plays a crucial role in the scattering of electromagnetic fields. An important deficiency in current research on microwave remote sensing of the ocean is the lack of detailed knowledge of the shape and time evolution of the ocean surface and how these quantities depend on the local wind field. In most cases, a statistical description of the surface is all that is available. Such a description is usually given in terms of the surface-height variance spectrum $S(\mathbf{k})$, where $\mathbf{k}$ is a two-dimensional wavenumber vector. The surface is modeled by a continuum of traveling wave components obeying the surface wave dispersion relation

$$\omega(\mathbf{k}) = \sqrt{gk\left[1 + \left(\frac{k}{k_0}\right)^2\right]\tanh kD} + \mathbf{k} \cdot \mathbf{V},$$

where g is the acceleration of gravity, D is the water depth, and $k_0 = \sqrt{\tau/\rho g}$, with τ being the surface tension and ρ the water density. The quantity $\mathbf{V}$ represents any additional background current (including orbital currents from longer surface wave components) that may be present. The phase speed of a particular wave component, $c_p(k)$, is just ω/k. From the preceding equation, the minimum value of $c_p(k)$ occurs for $k = k_0$, corresponding to a wavelength of about 17 cm. Most of our knowledge of $S(\mathbf{k})$ derives from point measurements of the waveheight frequency spectrum $S(\omega)$. For a surface where $S(\mathbf{k}) = S(k)$ (e.g., a one-dimensional surface), one can show that $S(k)$ and $S(\omega)$ are related by

$$S(k) = \frac{1}{k}\frac{d\omega}{dk}S(\omega),$$

where $d\omega/dk$ is the group velocity.

Several empirical models that parameterize $S(k)$ in terms of wind speed (or friction velocity) have been developed.[15,16] Figure 4 in the text shows plots of $S(k)$ versus k for the Bjerkaas–Riedel model[15] at various wind speeds. Note in Fig. 4 that as the wind speed increases, the spectral peak also increases in magnitude and moves to smaller k values (longer waves), and that the spectral density for higher k values (corresponding to wavelengths on the order of 10 cm or less) increases as well. This latter region of the spectrum, where the surface wave scales coincide roughly with the wavelengths of microwave radars, is particularly important in radar scattering calculations.

Even for the special case where $S(\mathbf{k}) = S(k)$, there are fundamental difficulties associated with inferring $S(k)$ from corresponding measurements of $S(\omega)$. These difficulties are caused by nonlinearities in the surface-wave hydrodynamics. A manifestation of these effects appears through the $\mathbf{k} \cdot \mathbf{V}$ term in the first equation. This term is generally nonzero because the surface velocity resulting from orbital motion of longer waves will shift the frequency of the shorter waves riding on them. Thus, since $d\omega/dk$ is a function of $\mathbf{V}$ as well as k, accurate measurements of $S(\omega)$ do not uniquely determine $S(k)$ unless $\mathbf{V}$ is also known.

The long-wave orbital surface current can also exchange energy with the short-scale waves through wave-current interaction processes. This mechanism, as well as wind stress variation over the long waves, can result in modulation of the short-scale spectral density as a function of position over the long-wave surface.[17] The basic idea is conceptualized in the accompanying figure, where we show the small-scale roughness to be largest near the crest on the downwind face of the longer waves. This type of nonhomogeneity of the short-wave spectrum skews the surface profile, creating wave crests that are sharper and higher than the troughs, and thus yield a non-Gaussian probability distribution for the surface elevation. Such non-Gaussian probability distributions are indeed observed experimentally (see, e.g., Ref. 18).
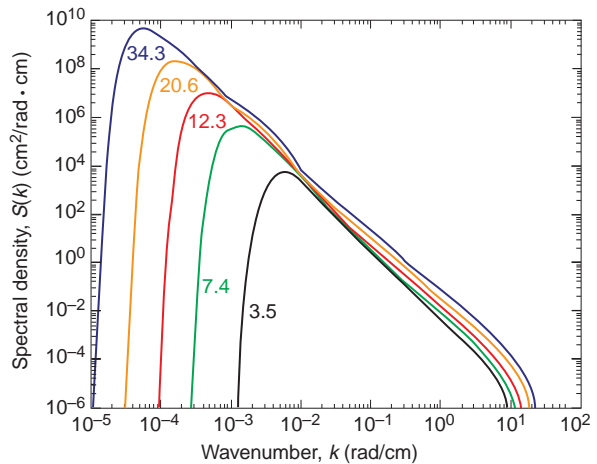
important omissions, such as the coupling between disparate length scales. Another limitation is that, by nature, it is an *averaged* representation and therefore ignores singular or transient effects such as breaking waves, whitecaps, dynamic wind-surface coupling, etc. Despite these difficulties with the spectral representation, our sea scattering simulations use the APL-developed Bjerkaas–Riedel spectrum[15] illustrated in Fig. 4. To generate random realizations of the ocean surface, this spectrum is discretized and substituted into Eq. 10 for $S(k_j)$.

Figure 5 shows a BMIA calculation (analogous to Fig. 3) of the averaged bistatic radar cross section from 80 realizations of a 2.7-m length of sea surface (wind speed, 10 m/s). The 3-cm wavelength incident radar beam is approximated by the tapered plane wave form and is incident at the near-grazing angle of 85°. It can

Figure 4. Sample calculation of the Bjerkaas–Riedel ocean wave-vector spectrum (co-wind) for various wind speeds (3.5–34.3 m/s). The surface wavelengths span 6 to 7 orders of magnitude from the longest gravity waves (small k) to the shortest capillaries (large k).

Therefore, accurate predictions of the radar cross section for microwave scattering from the ocean depend on an adequate description of the surface height statistics (which are usually non-Gaussian) or, equivalently, on a proper treatment of the nonhomogeneity of the short-wave spectrum.

Most of our knowledge of short-wave spectral modulation in the presence of longer waves has been obtained using microwave radars whose range cell is small compared with the wavelengths of the long waves. The accompanying schematic shows how these measurements may be obtained for backscatter geometry. Notice that in this description of the scattering process, we have implicitly divided the surface spectrum into long- and short-wave regions whose boundaries are roughly determined by the size of the range cell.
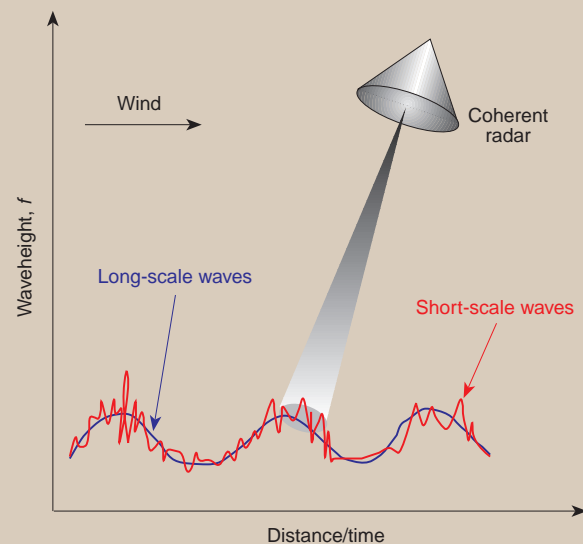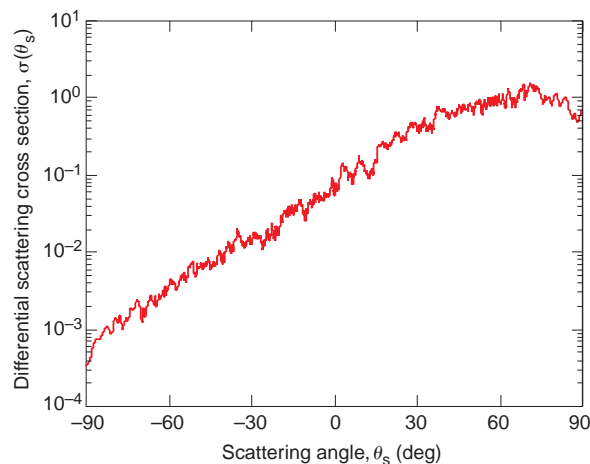

Composite surface schematic.

The long-wave portion of the spectrum is assumed homogeneous and stationary, whereas the short-wave portion varies slowly over the (long) spatial and time scales determined by properties of the long waves.

Basically, the backscattered field is sampled at a rate high enough to enable statistically significant estimates of the radar cross section in a time that is short compared with the period of the long-wave surface. For microwave radars whose range cell is on the order of 1 m and long waves whose wavelength is roughly 15 m or more, this time is about 0.25 s. (Since the field-decorrelation time for microwave radars is on the order of milliseconds, many independent samples may be collected over this sample time.) Furthermore, if the radars are coherent, measurements of the Doppler frequency of the scattered field can provide an estimate of the line-of-sight velocity of the long-wave surface that can be used to tag the cross-section measurements according to long-wave phase position.

Researchers at APL[19] have recently collected coherent microwave data of the type described here for comparison with predictions from an approximate time-dependent scattering model.[20] Using this model and a surface description similar to that previously outlined, we have been able to compute not only the time series of the cross section and Doppler spectrum of the (backscattered) electric field,[21] but also statistics of the field amplitude and phase.[19,22,23] The key assumption in these calculations is that the local (at a particular long-wave phase position) behavior of the short-scale surface waves can be described by a local (short-wave) spectrum with no higher-order terms. The higher-order moments arise entirely from modulation of the local spectrum as a function of long-wave phase position. An important objective of future work will be to couple the time-dependent surface description outlined here with the BMIA scattering technique. This will enable us to extend the calculations to high-incidence-angle regimes where the accuracy of more approximate methods is expected to decrease.

Figure 5. Calculation of the ensemble-averaged, normalized radar cross section from random realizations of the Bjerkaas–Riedel sea spectrum with a 10-m/s wind. The radar wavelength is 3 cm, and the beam is incident at 85° (near grazing).

be seen that for the choice of wavelength, wind speed, and incidence angle, the sea is a diffuse scatterer. The scattered power is greatest near the specular direction, but broadly distributed over all scattering angles, including the backscatter ($\theta_s < 0$) directions. The backscatter component ($\theta_s = -\theta_i = -85°$) characterizes the received signal strength for imaging radars or a source of noise for target detection and tracking.

When we compare Figs. 3 and 5, we see that at low grazing angle the moderately rough ocean scatters very differently from the Gaussian rough surface. This is primarily due to tilt, shadowing, and curvature effects of waves that are large compared with the radar's 3-cm wavelength. These effects vary randomly among realizations. The diffuse result shown in Fig. 5 is obtained after ensemble-averaging over the realizations or, equivalently, after time-averaging the radar return from a fixed

footprint on the sea surface. The ocean surface realizations used for Fig. 5 have an rms height about 3 times larger than the Gaussian surfaces used for Fig. 3. Most of the excess wave energy is in the longer waves (with large correlation length), which are not present in the Gaussian rough surfaces. Thus, rough surfaces with Gaussian spectra poorly approximate sea surface scattering.

In Fig. 6, the radar backscatter cross section is shown as a function of wind speed for three incidence angles. At near-grazing incidence ($\theta_i = 80°$), the cross section strongly increases with wind speed because of both increasing small-scale roughness on the surface and a broader distribution of surface slopes (larger tilts). Interestingly, at near-normal incidence (15°) the cross section is nearly independent of wind speed, an effect that has been observed experimentally.[24] We have also verified that at even higher incidence angles, where the backscatter is mostly due to specular reflection, the cross section *decreases* with wind speed, as one expects from the broader distribution of surface slopes. Figure 6 also gives some information on the incidence angle dependence of radar backscatter. At a 10-m/s wind, for example, the cross section increases by 2 orders of magnitude, from 80° to 40° incidence. The cross section increases at a similar rate until about 20° and then levels off approaching normal incidence.

To further quantify the performance of our BMIA code, we list in Table 1 the computational parameters for calculations similar to those shown in Fig. 5 but using $\theta_i = 40°$. With a surface length of 2.7 m, wavelength of 3 cm, and sampling rate of 20 points per wavelength, the problem requires $N = 1800$ samples. Column 1 lists various bandwidths b for the strong

interaction matrix. As the bandwidth increases, the computational efficiency of the banded matrix method decreases. At $b = 401$, for example, a single-grid calculation on one realization of the surface requires 14 MB of memory and 5.9 computing min. The multigrid method reduces the memory requirement to 6 MB, but the extra overhead increases computing time slightly. As b increases, substantial reductions are achieved in both time and memory. For completeness, Table 1 includes the calculated energy conservation index defined in the previous section. In each case, energy is conserved to four decimal places.

Table 1. Computational performance of the BMIA code for calculations similar to those in Fig. 5.

Bandwidth	Computer time (min)	Memory (MB)	Energy conservation index
401	(5.9, 7.0)	(14.0, 6.0)	(1.0001, 1.0001)
801	(12.1, 10.8)	(28.0, 6.5)	(0.9998, 0.9998)
1001	(16.7, 12.9)	(35.0, 7.0)	(0.9999, 0.9999)

Note: Pairs in parentheses represent single-grid calculations on the left and multigrid calculations on the right.

SUMMARY

With its exceptional computational efficiency, the BMIA is a powerful new tool for surface scattering simulation, enabling the solution of large-scale problems that were previously unapproachable. This new capability is particularly promising for the study of diffuse radar scatter from the ocean, a long-standing problem of great interest to APL, its sponsors, and radar and remote sensing researchers. Simulations were shown of 10-GHz radar scatter from a model ocean surface, at various incidence angles and wind speeds. The calculations confirm our physical intuition in several cases, and in general enable us to quantify order-of-magnitude effects that are of fundamental importance to several Laboratory programs, including a model for low-grazing-angle radar propagation over the ocean (the Troposphere Electromagnetic Parabolic Equation Routine model).

Significant progress has been made in sea-scatter modeling, although substantial challenges remain. For example, the current model is valid only for Dirichlet boundary conditions, or the equivalent of a horizontally polarized electric field incident on a perfectly conducting surface. Although this is considered a reasonable approximation for horizontal polarized sea scatter, the perfect conductivity assumption is generally inadequate
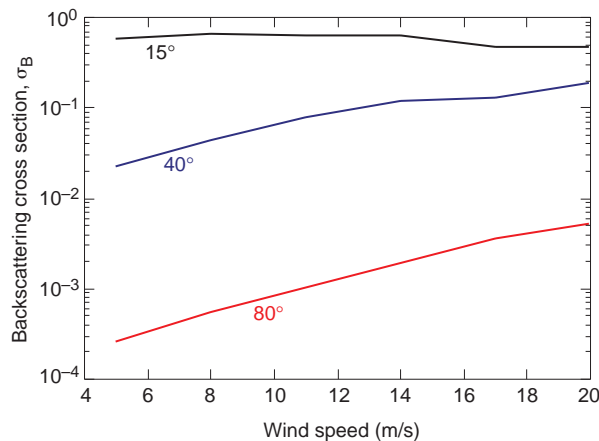

Figure 6. Calculation of the ensemble-averaged, normalized backscatter cross section from random realizations of the Bjerkaas–Riedel spectrum. The results are shown as a function of wind speed for near-normal (15°), moderate (40°), and near-grazing (80°) incidence angles.

for vertical polarization at radar frequencies. As a result, a lossy surface will have to be introduced.

In addition to polarization and surface conductivity effects, a full three-dimensional scattering model is also a high priority. Such a model will incorporate scattering contributions into and out of the plane of incidence and will also remove the restriction of cylindrical surface roughness. Given the enormous computational complexity of the radar/ocean surface problem, direct numerical simulations in three dimensions have not been considered possible until very recently. Because of its efficiency, the banded matrix approach we have developed may be especially well-suited to this challenging problem.

Finally, as the capability of the simulation is expanded, improved calculations will also require more refined hydrodynamic modeling of the ocean surface. Ocean hydrodynamics is itself an active area of research, with much left to be learned. We are currently developing a two-scale decomposition of the ocean surface in which the longer waves are propagated deterministically and contribute a time-dependent mean tilt to the small-scale random surface realization. Methods for coupling the large and small scales (see the insert, Ocean Surface Hydrodynamics) are also being considered.

REFERENCES

[1] Ogilvy, J. A., *Theory of Wave Scattering from Random Rough Surfaces*, Adam Hilger, New York (1991).
[2] Kaczkowski, P. J., *A Study of the Operator Expansion Method and Its Application to Scattering from Randomly Rough Dirichlet Surfaces*, APL-UW TR9406, Univ. of Washington Applied Physics Laboratory, Seattle, WA (1994).
[3] Stoyanov, B. J., and Farrell, R. A., "Schwinger Variational Principle Calculations of Wave Scattering from Conducting Cylinders Using Physically Motivated Trial Functions," *Phys. Rev. E* **53**, 1907–1916 (1996).
[4] Freund, D. E., and Farrell, R. A., "A Variational Principle for the Scattered Wave," *J. Acoust. Soc. Am.* **87**, 1847–1860 (1988).
[5] Donohue, D. J., *Application of a Stochastic Variational Principle to Random Rough Surface Scattering*, JHU/APL RTB-001-94, Laurel, MD (1994).
[6] Harrington, R. F., *Field Computation by Moment Methods*, Macmillan, New York (1968).
[7] Tsang, L., Chan, C. H., Pak, K., and Sangani, H., "Monte-Carlo Simulations of Large-Scale Problems of Random Rough Surface Scattering and Applications to Grazing Incidence with the BMIA/Canonical Grid Method," *IEEE Trans. Antennas Propagat.* **43**, 851–859 (1995).
[8] Nussbaumer, H. J., *Fast Fourier Transform and Convolution Algorithms*, Springer Verlag, Berlin (1981).
[9] Hackbush, W., *Multi-Grid Methods and Applications*, Springer, Berlin (1985).
[10] Brandt, A., "Multi-Level Adaptive Solutions to Boundary-Value Problems," *Math. Comput.* **31**, 333–390 (1977).
[11] Wesseling, P., *An Introduction to Multigrid Methods*, John Wiley & Sons, London, England (1992).
[12] Wong, Y. S., Zang, T. A., and Hussaini, M. Y., "Preconditioned Conjugate Residual Methods for the Solution of Spectral Methods," *Comput. Fluids* **14**, 85–89 (1986).
[13] Thorsos, E. I., "The Validity of the Kirchhoff Approximation for Rough Surface Scattering Using a Gaussian Roughness Spectrum," *J. Acoust. Soc. Am.* **83**, 78 (1988).
[14] Ishimaru, A., "Backscatter Enhancement: From Radar Cross Sections to Electron and Light Localizations to Rough Surface Scattering," *IEEE Antennas Propagat. Mag.* **33**(5), 7–11 (1991).
[15] Bjerkaas, A. W., and Riedel, F. W., *Proposed Model for the Elevation Spectrum of a Wind-Roughened Sea Surface*, JHU/APL TG-1328, Laurel, MD (1979).
[16] Apel, J. R., "An Improved Model of the Ocean Surface Wave Vector Spectrum and Its Effects on Radar Backscatter," *J. Geophys. Res.* **99**, 16,269–16,291 (1994).
[17] Plant, W. J., "The Modulation Transfer Function: Concept and Applications," in *Radar Scattering from Modulated Wind Waves*, G. J. Komen and W. A. Oost (eds.), pp. 155–172, Kluwer Academic Publishers, Boston (1989).
[18] Phillips, O. M., *The Dynamics of the Upper Ocean*, Cambridge University Press, New York (1977).
[19] Gotwols, B. L., and Thompson, D. R., "Ocean Microwave Backscatter Distributions," *J. Geophys Res.* **99**, 9741–9750 (1994).
[20] Thompson, D. R., "Doppler Spectra from the Ocean Surface with a Time-Dependent Composite Model," in *Radar Scattering from Modulated Wind Waves*, G. J. Komen and W. A. Oost (eds.), pp. 27–40, Kluwer Academic Publishers, Boston (1989).
[21] Thompson, D. R., Gotwols, B. L., and Keller, W. C., "A Comparison of K_u-Band Doppler Measurements at 20° Incidence with Predictions from a Time-Dependent Scattering Model," *J. Geophys. Res.* **96**, 4947–4955 (1991).
[22] Chapman, R. D., Gotwols, B. L., and Sterner, R. E. II, "On the Statistics of the Phase of Microwave Backscatter from the Ocean Surface," *J. Geophys. Res.* **99**, 16,293–16,303 (1994).
[23] Thompson, D. R., and Gotwols, B. L., "Comparison of Model Predictions for Radar Backscatter Amplitude Probability Density Functions with Measurements from SAXON," *J. Geophys. Res.* **99**, 9725–9739 (1994).
[24] Wetzel, L. B., "Sea Clutter," Chap. 13, in *Radar Handbook*, 2nd Ed., M. I. Skolnik (ed.), McGraw Hill, New York (1990).

THE AUTHORS

DENIS J. DONOHUE received a B.A. in computer science from Rutgers University in 1985 and a Ph.D. in electrical engineering from Stanford University in 1991. Following a postdoctoral appointment in space plasma physics, he joined APL's Milton S. Eisenhower Research and Technology Development Center in 1993, where he is currently a member of the Physics, Modeling, and Applications Group. Dr. Donohue's research interests span a broad range in space science and astrophysics, optics, acoustics, and electromagnetic theory. Common themes underlying all of his work are the interaction of waves (electromagnetic, acoustic, plasma) with matter and the use of computational methods as tools for analytical research. His e-mail address is Denis.Donohue@jhuapl.edu.

HWAR-CHING KU received a B.S. from Tsing Hua University in 1976, an M.S. from Taiwan University in 1978, and a Ph.D. from Illinois Institute of Technology in 1984, all in chemical engineering. He came to APL in 1985 as a research associate and is now in the Physics, Modeling, and Applications Group of the Milton S. Eisenhower Research and Technology Development Center and became senior staff in 1987. Most of his recent research interests include numerical methods in computational fluid dynamics, magnetohydrodynamics in space physics, and electromagnetic surface scattering. His e-mail address is Hwar.Ku@jhuapl.edu.

DONALD R. THOMPSON received a B.S. in physics from Case Western Reserve University in 1964 and a Ph.D. in theoretical physics from the University of Minnesota in 1968. Dr. Thompson spent 2 years studying problems in stellar nucleosynthesis at the California Institute of Technology before returning to the University of Minnesota in 1970. From 1976 to 1978, he was an Alexander von Humboldt Fellow in the Institut für Theoretiche Physik at the Universität Tübingen in Germany. Since coming to APL in 1980, Dr. Thompson's research has focused on the physics of ocean surface waves and electromagnetic scattering from the ocean surface. He is currently supervisor of the Theory and Modeling Section of the Space Oceanography Group. His e-mail address is Donald.Thompson@jhuapl.edu.
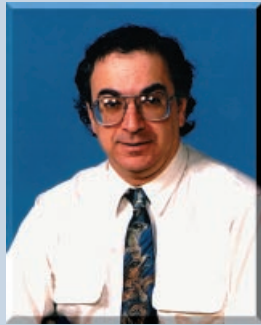
JOHN SADOWSKY is the assistant supervisor of the Advanced Signal and Information Processing Group of the Milton S. Eisenhower Research and Technology Development Center at APL. He earned a B.A. in mathematics from The Johns Hopkins University in 1971 and a Ph.D. in mathematics from the University of Maryland in 1980. His work includes advanced transforms and algorithms for signal processing and, in collaboration with researchers in The Johns Hopkins University Schools of Engineering, Arts and Sciences, and Medicine, he coordinates the Sensory Engineering Program. Before joining APL in August 1989, he was a principal scientist and supervisor at the Systems Engineering and Development Corporation (now a division of the Essex Corporation), where he led programs to develop advanced transforms, algorithms, and architectures for processing systems for electronic and communication signals intelligence. His e-mail address is John.Sadowsky@jhuapl.edu.